


Article

Numerical Analysis of Perforated Symmetric Fissures on Mechanical Properties of Hole-Containing Sandstone

Hong Gou ^{1,2}, Peng Shi ^{1,2}, Zhijun Wan ^{1,2,*}, Luchang Xiong ^{1,2} , Bowen Fan ^{1,2} and Zheng Zhen ^{1,2}

¹ Key Laboratory of Deep Coal Resource Mining (CUMT), Ministry of Education of China, Xuzhou 221116, China; ts21020012a31tm@cumt.edu.cn (H.G.); tb22020024a41@cumt.edu.cn (P.S.); lchxiong@cumt.edu.cn (L.X.); ts20020012a31tm@cumt.edu.cn (B.F.); ts22020073a31ld@cumt.edu.cn (Z.Z.)

² School of Mines, China University of Mining & Technology, Xuzhou 221116, China

* Correspondence: zhijwan@cumt.edu.cn

Abstract: The symmetrical fissures located within the surrounding rock of the roadway (borehole) in tunnel engineering activities can easily induce damage and instability of the surrounding rock. Therefore, studying the impact of perforated symmetrical fissures on the mechanical properties of rock with a hole has significant practical significance. Based on indoor experimental results, conventional triaxial compression simulations were performed on symmetrical fissure-hole sandstone using PFC2D. The impact of the dip angle and length of symmetric fissures on the mechanical properties of the hole-containing sandstone was analyzed. Furthermore, the relationship between crack propagation and the macroscopic mechanical properties of the specimen was discussed. The results show that: (1) The deterioration effect of symmetric fissures on hole-containing sandstone can be controlled by increasing the fissure dip angle, suppressing the stress drop phenomenon. However, increasing the fissure length exacerbates the deterioration effect. (2) The effect of symmetrical fissure dip angle on the displacement field near the hole decreases with increasing dip angle while increasing fissure length exacerbates the effect of fissures on the displacement field. (3) As the angle between the fissure and the vertical principal stress increases, the degree of tensile failure weakens while the degree of shear failure increases. (4) During the crack development phase, the extension of the stress concentration zone drives rapid crack growth. It exhibits a stress drop in the macroscopic mechanical properties, followed by the evolution of the stress field with loading, allowing rapid expansion of the microcracks and eventually leading to rock destabilization damage.

Keywords: symmetric fissures; hole; mechanical properties; particle flow simulation



Citation: Gou, H.; Shi, P.; Wan, Z.; Xiong, L.; Fan, B.; Zhen, Z. Numerical Analysis of Perforated Symmetric Fissures on Mechanical Properties of Hole-Containing Sandstone. *Appl. Sci.* **2023**, *13*, 8780. <https://doi.org/10.3390/app13158780>

Academic Editors: Andrea L. Rizzo and Tiago Miranda

Received: 17 June 2023

Revised: 26 July 2023

Accepted: 27 July 2023

Published: 29 July 2023



Copyright: © 2023 by the authors. Licensee MDPI, Basel, Switzerland. This article is an open access article distributed under the terms and conditions of the Creative Commons Attribution (CC BY) license (<https://creativecommons.org/licenses/by/4.0/>).

1. Introduction

Defects, including fissures, holes, and joints of various sizes and types, are frequently observed within the surrounding rock of roadways (boreholes) during tunnel engineering activities. The spatial distribution and geometry of these defects significantly impact the mechanical properties of the roadway's surrounding rock [1,2]. Extensive research conducted by scholars both domestically and internationally has demonstrated that defects play a pivotal role in inducing damage to the surrounding rock of roadways [3–5]. To enhance the control effectiveness of the roadway's surrounding rock-containing defects, it is imperative to understand the influence mechanisms of different defect forms on the mechanical properties and damage modes of rock masses containing boreholes. Consequently, researchers have comprehensively investigated the mechanical behavior, damage evolution, and crack propagation characteristics of rock masses featuring holes, fissures, and other defects (in this paper, the term “fissure” is used to denote a pre-existing crevice defect in the rock, and the term “crack” is used to denote cracks and damages that occur during loading).

In indoor experiments, the literature [6–13] explores rock samples' mechanical properties and crack propagation characteristics with prefabricated fissures or holes under

compression loading. Yang [14] investigated the mechanical properties of sandstone with holes and fissures in uniaxial compression and found that the strength of the sandstone was affected by hole diameter and defect symmetry. Modiriasari [15] monitored the cracking behavior of specimens using digital image correlation (DIC) and acoustic emission. Zhu [16] introduced a combination defect of circular holes and single fissures within a sandstone slab. They discovered that the strength parameters of the combined defective sandstone under uniaxial compression decreased as the dip and length of the fissure increased. Several researchers have conducted numerical simulations to understand the mechanical behavior of rock masses containing defects such as fissures, holes, and joints. Li [17] used the granular flow program PFC2D (Particle Flow Code 2D) to simulate uniaxial compression for sandstones with hole-type trident fissures. Their study revealed that the fissure length had the most significant effect on the peak strength of rock samples with this type of defect. Aliabadian [18] investigated the applicability of DIC and the granular flow model (Bonded Particle Model) to the mechanical behavior of natural rock masses containing defects. They found that the Bonded Particle Model (BPM) accurately simulated the location of crack initiation and the type of agglomeration detected by DIC. Sharafisafa [19] compared the effectiveness of DEM (Discrete Element Method) and XFEM (Extended Finite Element Method) in simulating crack sprouting and extension in jointed rock masses. Their research showed that DEM could simulate all cracks during rock fracture, while XFEM could only simulate wing cracks (a crack pattern that extends outward in an arch on both sides of the crack). Wang [20] and Yao [21] performed uniaxial compression numerical simulations of rock masses containing defects of different morphologies and types using PFC2D, demonstrating that the fissure angle could alter the specimen's internal stress field, affecting the rock mass's mechanical properties.

The synthesis of previous studies reveals that numerous authors have conducted in-depth discussions on the geometric form and spatial distribution of fissures surrounding boreholes, including aspects such as the number, length, angle, and distance of these fissures. However, there is a relative scarcity of systematic investigations focusing on the impact of perforated symmetrical fissures on rock masses containing boreholes, despite observations of near-symmetrical perforated fissures during engineering practice, as depicted in Figure 1. Furthermore, in conventional triaxial compression tests, particle flow simulation exhibits tremendous advantages in identifying crack types and monitoring the sequential extension of cracks compared to indoor tests. Building upon these insights, a perforated symmetric fissures-hole model is constructed by simplifying the morphology of near-symmetric perforated fissures. Subsequently, the effect of this perforated symmetric fissure morphology on the mechanical properties of sandstone-containing boreholes is primarily examined through numerical simulations of the particle flow process.

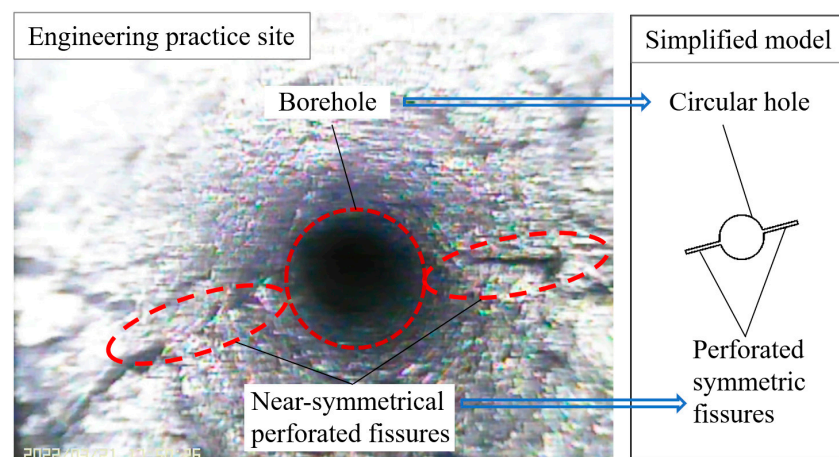


Figure 1. Engineering practice field and theoretical simplified models.

This paper initiates with uniaxial compression tests conducted on perforated symmetric fissures-hole sandstones. Subsequently, microscopic parameters were calibrated based on the results obtained from the indoor tests [22]. The reasonableness of these microscopic parameters was further verified by comparing damage modes. Building upon this foundation, a simulation study employing conventional triaxial compression was carried out on sandstone specimens featuring fissures of varying dip angles and lengths using PFC2D. The investigation focused on analyzing the mechanical properties, damage modes, and crack propagation characteristics of hole-containing sandstone under the influence of perforated symmetric fissures, with a view to providing some reference values for related projects.

2. Construction of a Numerical Model of Particle Flow

2.1. Introduction to Particle Flow Code Simulation Methods

Particle Flow Code 5.0 (PFC 5.0) is an essential discrete element numerical simulation software developed by ITASCA, Itasca, IL, USA [23]. It has been extensively utilized to study fundamental problems such as rock-like materials' basic mechanical properties, particulate matter's dynamic responses, and fracture development. The macroscopic mechanical behavior of materials in PFC is determined by the type of contact between particles and their variation characteristics.

The Linear model, as implemented in the PFC, represents the fundamental contact model in rock mechanics. It characterizes the mechanical behavior of contact surfaces through parallel spring and damper elements. However, it should be noted that the Linear model solely facilitates the transfer of forces (F) and does not account for moments (M). The Linearpbond model (Linear Bond Model), which is one of the common granular models in PFC, was developed within the PFC framework to address this limitation. By incorporating bonding capabilities into the Linear model, the Linearpbond model enables the transmission of both forces (F) and moments (M), as depicted in Figure 2. In this model, the bonding elements and spring elements are parallel to each other, and the maximum normal stress (σ_{max}) and shear stress (τ_{max}) around the parallel bond in the two-dimensional plane are defined as [24]:

$$\sigma_{max} \leftarrow F_n / A + M_b \bar{R} / I \quad (1)$$

$$\tau_{max} \leftarrow F_s / A \quad (2)$$

$$F_n \leftarrow F_n + k_n A \Delta \delta_n \quad (3)$$

$$F_s \leftarrow F_s + k_s A \Delta \delta_s \quad (4)$$

$$M_b \leftarrow M_b + k_b \Delta \theta_b \quad (5)$$

$$\bar{R} = \bar{\lambda} \min(R_1, R_2) \quad (6)$$

$$I = \frac{2}{3} \bar{\lambda}^3 \quad (7)$$

where A is the area, F_n is the normal force, F_s is the shear force, M_b is the bending moment, \bar{R} is the bond radius, I is the moment of inertia of the parallel bond cross-section, k_n , and k_s are the normal and shear stiffnesses, respectively, $\Delta \delta_b$ and $\Delta \delta_s$ are the displacement increments in the normal and tangential directions respectively, R_1 and R_2 are the particle radius, $\Delta \theta_b$ is the contact angle, and $\bar{\lambda}$ is the radius factor.

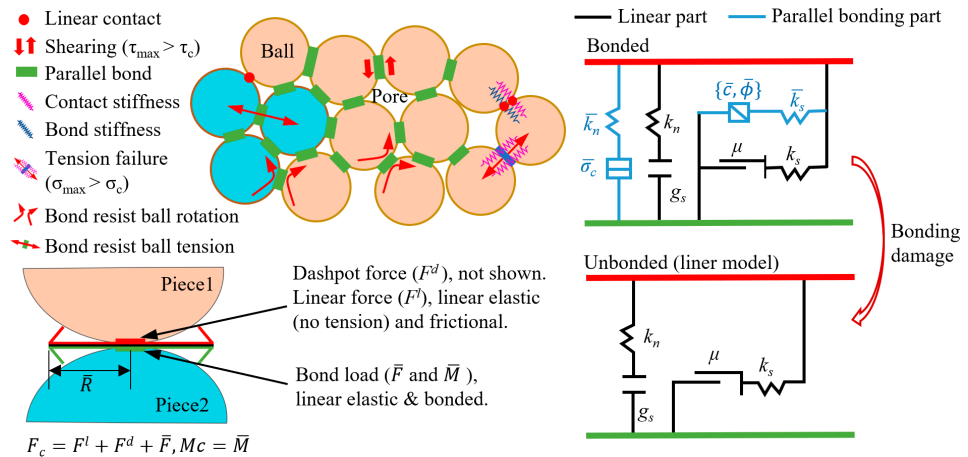


Figure 2. Principle of linear parallel bonded contact model [24].

The strength properties of the parallel bond adhere to the Moore-Coulomb criterion. When the forces (F) or moments (M) exerted on the contact surfaces attain their maximum strength, the bond undergoes failure, causing the Linearpbond model to transition from a bonded state to an unbonded state. Notably, in its unbonded state, the Linearpbond model aligns completely with the Linear model [25]. The linear parallel bond contact model represents the parallel bond as a bonding material characterized by constant stiffness (both normal and shear) and strength between two particles. This model is commonly utilized to simulate the discontinuous deformation of rock formations. Previous studies conducted on rock materials using the Particle Flow Code (PFC) have demonstrated that employing a linear parallel bond contact model between particles yields a more accurate representation of rocks’ mechanical properties and particulate media’s dynamic response [26,27]. Consequently, this paper adopts the linear parallel bond contact model for the numerical simulation of particle flow.

2.2. Model Building

In order to investigate the effect of symmetrical fissure dip angle and length on the mechanical properties of hole-containing sandstones under conventional triaxial compression, a two-dimensional numerical model of particle flow was established with the standard cylindrical specimen (50 mm × 100 mm) longitudinal cross-sectional dimensions, and defects in the model were achieved by deleting particles, as shown in Figure 3. Symmetrical fissures of differing lengths and dip angles were prefabricated in the model and penetrated a single circular hole located at the model’s center. The settings for some of the model parameters are presented in Table 1. Four walls were generated around the model, while σ_1 was loaded axially for the top and bottom loading walls, and σ_3 was loaded transversely for the left and right servo walls. The loading method was displacement-controlled, with a loading rate of 0.02 mm/s. The axial loading pressure is set to stop when it is reduced to 70% of the peak strength of conventional compression, and a total of 29 different working conditions are simulated.

Table 1. Model parameters.

Parameters	Numerical Values
Number of particles	11137
Hole diameter (d)	10 mm
Fissure width	0.8 mm
Fissure length (2a)	0 mm, 4 mm, 8 mm, 12 mm, 16 mm
Fissure dip angle (α)	0°, 15°, 30°, 45°, 60°, 75°, 90°

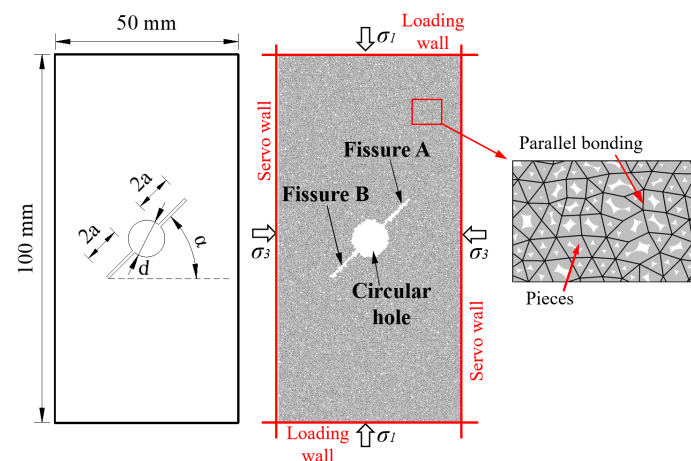


Figure 3. Model settings and linear parallel bond model.

3. Calibration and Verification of Model Mesoscopic Parameters

3.1. Calibration of Mesoscopic Parameters

Accurate numerical simulations require the precise determination of microscopic parameters. In the Particle Flow Code 2D (PFC2D), the mesoscopic parameters of the linear parallel bond contact model encompass particle parameters and bonding parameters. The particle parameters primarily comprise the particle size range, particle size ratio (R_{max}/R_{min}), particle density (ρ), particle stiffness ratio (k), radius factor ($\bar{\lambda}$), particle dissipation energy ($Damp$), particle friction coefficient (μ) and particle Young's modulus (E). On the other hand, the critical microscopic parameters pertaining to parallel bonding include the bond strength (pb_s_t), bond stiffness ratio (pb_k), bond Young's modulus (pb_E), and bond cohesion (c) [28]. The primary difference between the uniaxial compression in PFC2D and conventional triaxial compression lies in whether or not the left and right servo walls are required to provide the surrounding pressure. However, the microscopic parameters in the linear parallel bond model serve mainly for specimen formation and rock bonding, which are partially the same in uniaxial and conventional triaxial compression. Therefore, uniaxial compression indoor tests and simulations were carried out for perforated symmetrical fissure-hole sandstone specimens tested at $\alpha = 15^\circ, 45^\circ$ and 75° . By systematically adjusting the microscopic parameters based on the macroscopic mechanical responses observed during indoor experiments [22], a set of microscopic parameters that accurately reflect the mechanical behavior of the selected perforated symmetrical fracture-hole sandstone specimens was obtained. This iterative process ensured that the simulated behavior closely matched the experimental results, enhancing the fidelity of the numerical modeling approach.

The sandstone specimens loaded indoors were taken from Pingdingshan City, Henan Province, China, and consisted mainly of two minerals, quartz, and feldspar, and some geomechanical characteristics of the intact sandstone specimens are shown in Table 2. The specimens were brittle, and the holes were machined to a small size to prevent damage to the specimens during hole processing, and the size parameters of each defect are shown in Table 3. The indoor test system is shown in Figure 4. Uniaxial compression tests were carried out using the ZTR-276 rock triaxial test system with a displacement control method and a loading rate of 0.02 mm/s. For the simulation tests, the model size, defect size, and loading settings were replicated from the indoor tests. Subsequently, the microscopic parameters of the model underwent iterative adjustment using a 'trial and error' approach until the macroscopic mechanical behavior of the specimen in the simulation results closely matched that observed in the indoor uniaxial compression test results. The refined microscopic parameters selected at the end of this iterative process are presented in Table 4.

Table 2. Partial geomechanical characteristics of the selected intact sandstone specimen.

Parameters	Compressive Strength (MPa)	Elastic Modulus (GPa)	Natural Density (kg/m ³)	Saturated Density (kg/m ³)	Porosity (%)
Values	75.92	38.87	2.51 × 10 ³	2.65 × 10 ³	1.6%

Table 3. Defect size parameters of uniaxial compression specimens.

Sample Number	d (mm)	2a (mm)	Fissure Width (mm)	α (°)
D-1	5.0	7.1	2.5	75
D-2	5.1	7.0	2.5	45
D-3	5.0	7.0	2.5	15

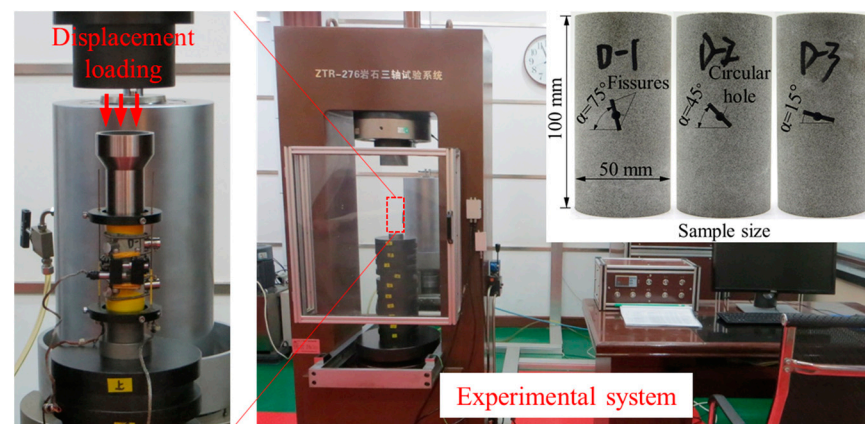


Figure 4. Indoor test loading system and samples.

Table 4. PFC2D mesoscopic parameters.

Mesoscopic Parameters	Value	Mesoscopic Parameters	Value
Particle size range, (mm)	0.2~0.3	Particle friction coefficient μ	0.5
Particle size ratio R_{max}/R_{min}	1.5	Particle Young's modulus E (GPa)	50
Particle density ρ , (kg/m ³)	2500	Bond strength pb_{σ_t} (MPa)	10
Particle stiffness ratio k	2.0	Bond stiffness ratio pb_k	2.0
Radius factor $\bar{\lambda}$	1.0	Bond Young's modulus	
Particle dissipation energy $Damp$	0.7	pb_E (GPa)	50

Figure 5 compares the mechanical properties of the results simulated through the microscopic parameters in Table 4 and the indoor test results. In Figure 5a, the stress-strain curve of the indoor test can be divided into four distinct stages: the compaction stage, elastic stage, plastic stage, and failure stage. During the plastic phase, a significant drop in stress magnitude is negatively correlated with the fissure dip. This finding aligns with the test results reported by Yang [14]. This is due to the lower load-bearing properties of the rock near the defect, which makes it more likely to fracture and sprout cracks during the loading process.

Moreover, at $\alpha = 15^\circ$, a double peak appears in the stress-strain curve, which may be attributed to the horizontal orientation of the fissure, which leads to its closure under pressure during loading. As a result, the specimen exhibits a substantial load-bearing capacity even after experiencing partial damage. Figure 5b illustrates that the peak strength and modulus of elasticity of the perforated symmetric fissure-hole sandstone specimens demonstrate varying degrees of reduction compared to the macroscopic mechanical parameters of the intact sandstone specimens outlined in Table 2. Moreover, the specimens' peak strength and elastic

modulus decrease as α decreases. These observed phenomena indicate that the presence of symmetric fissure-hole combination defects deteriorates the mechanical properties of the sandstone. Specifically, the dip angle (α) of the perforated symmetric fissure impacts the mechanical properties of hole-containing sandstone under uniaxial compression, with lower dip angles corresponding to a higher likelihood of rock damage.

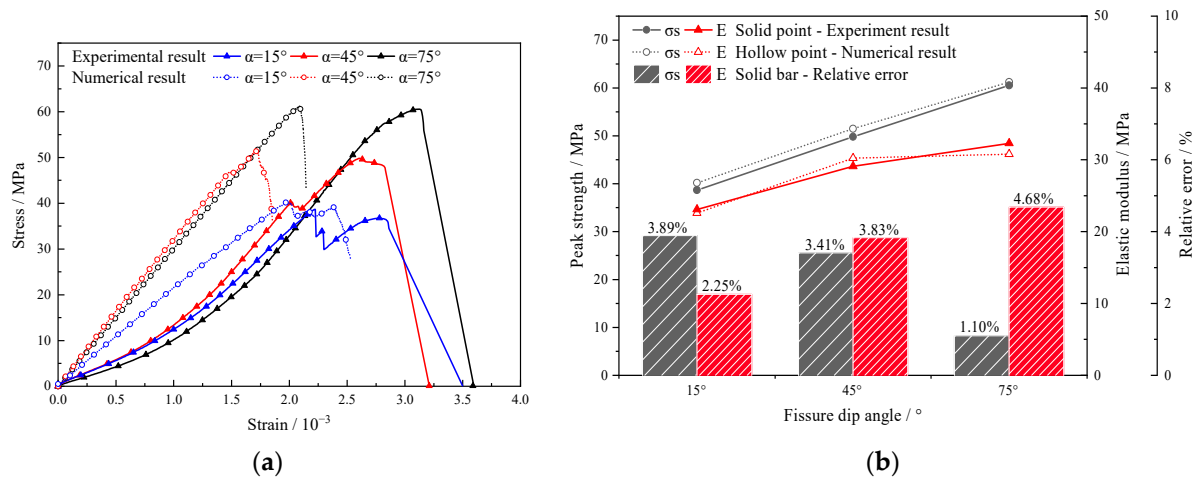


Figure 5. Comparison of mechanical properties between indoor test and numerical simulation. (a) Comparison of stress-strain curves; (b) comparison of peak strength and elastic modulus.

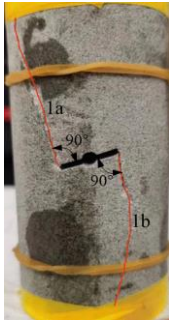
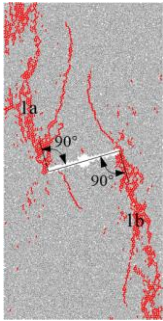
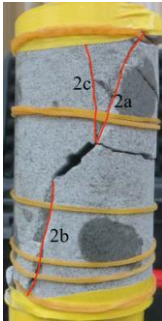
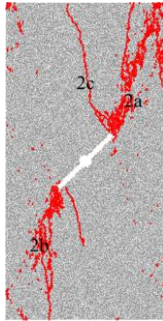
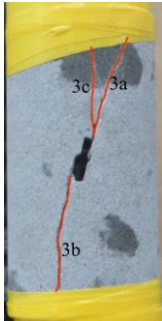
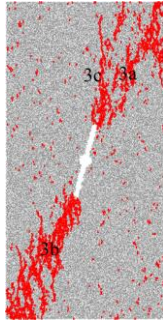
The stress-strain curves obtained through numerical simulations of various specimens are highly comparable to the results of indoor testing. The curves obtained from indoor tests and simulations exhibit a consistent trend, with a close agreement in terms of both the slope of the elastic phase and the peak values. However, it is worth noting that due to the rigid nature of the model particles and their close proximity, the simulated specimens enter the elastic phase at the onset of the loading stage. Consequently, the initial compaction phase, observed in the experimental curve, is absent in the simulated curve. This disparity causes a leftward shift of the simulated curve relative to the experimental curve. Peak strength and elastic modulus also closely resemble the two data sets, with both increasing as the fissure dip angle increases (as shown in Figure 5b). The errors in peak strength between the numerical simulation and indoor tests ranged from 1.10% (0.66 MPa) to 3.89% (1.5 MPa), while the errors in modulus of elasticity ranged from 2.25% (0.52 GPa) to 4.68% (1.51 MPa). These discrepancies indicate that the numerical simulation results agree with the test results. Therefore, the microscopic parameters selected in Table 4 are reasonable and reliable.

3.2. Verification of Mesoscopic Parameters

Table 5 compares the failure modes observed during indoor uniaxial compression tests and numerical simulations, providing additional validation of the selected microscopic parameters. In the table, numerical letters (e.g., 1a) in both test and simulation results refer to macrocracks initiating specimen failure. It is clear from the table that the prominent macroscopic cracks on the surface of specimens observed during indoor testing corresponded one-to-one with the simulation results, and the damage patterns were similar. At $\alpha = 15^\circ$, the primary cracks (1a and 1b) extending from fissure tips grew perpendicularly, eventually causing tension-shear failure at the specimen's top left and bottom right corners. Similarly, at $\alpha = 45^\circ$, primary cracks (2a and 2b) originating from fissure tips penetrated both the fissure and the specimen edge, while a secondary crack (2c) extended from the fissure tip to the specimen's top surface. Due to the anisotropic nature of the sandstone samples, certain forms of crack propagation differed between the indoor test and numerical simulation; however, the outcome was still mixed tensile-shear failure. At $\alpha = 75^\circ$, the fissure tip experienced primary cracks (3a and 3b) and a secondary crack (3c), which

extended from the bottom left to the top right corners of the specimen, causing pure shear failure. The direction of the failure zone is approximately parallel to the fracture direction.

Table 5. Comparison of failure modes between indoor experiment and numerical simulation.

Fissure Dip Angle (°)	15°		45°		75°	
	Experimental Result	Numerical Result	Experimental Result	Numerical Result	Experimental Result	Numerical Result
Failure modes						

Through a comparison between indoor experiments and numerical simulations, it can be concluded that the mechanical characteristic parameters of the specimens are highly consistent, as well as the crack propagation pattern and failure mode. Therefore, the group of microscopic parameters can be employed to simulate the mechanical characteristics of symmetrical fissure-hole sandstone accurately. This group of parameters can also be utilized to analyze the effects of different fissure morphologies on the mechanical properties of hole-containing sandstone under conventional triaxial compression.

4. Numerical Simulation Results and Analysis

4.1. Characterization of Mechanical Parameters

Figure 6 illustrates the stress-strain curves of symmetrical fissure-hole sandstone specimens. As the influence of fissure dip on the stress-strain curves was consistent across all specimens, only the curve for specimens with a fissure length of 8 mm is presented in the figure. Figure 6a shows the stress-drop phenomenon before the peak stress occurs at different magnitudes when the fissure dip angle ranges from 0° to 45°. Figure 6b reveals a decreasing trend in stress drop as α increases. This suggests that increasing the fissure dip angle can reduce the stress drop effect, as observed in the indoor experiment (Section 2.2). The cause of the stress drop was analyzed to be the change in stress distribution within the specimens due to the variation in the fissure dip angle. When the angle between the fissure and the axial principal stress direction was larger, stress concentration at the fissure tips was more intense, as demonstrated in Jiang's study [26] on force chain distribution near the fissure.

The relationship between the symmetrical fissure dip angle and the strength parameters of the hole-containing sandstone is depicted in Figure 7. An increase in fissure dip angle results in higher peak strength and elastic modulus values for the specimens, which gradually converge towards those of the non-fissure specimen. In addition, as the fissure dip angle increases, the specimens' peak strength and elastic modulus demonstrate a gradual, rapid, and then gradual growth trend. This trend is particularly pronounced when α ranges from 30° to 75°; with a dip angle of 45°, the elastic modulus demonstrates the fastest rate of growth. Therefore, the presence of perforated symmetric fissures worsens the mechanical properties of hole-containing sandstones, while increasing the angle of the fissures helps to mitigate the worsening effect. The sensitivity of the specimens' mechanical properties to changes in fissure dip angle is highest within the range of 30° to 75°, with the most sensitive point being around 45°.

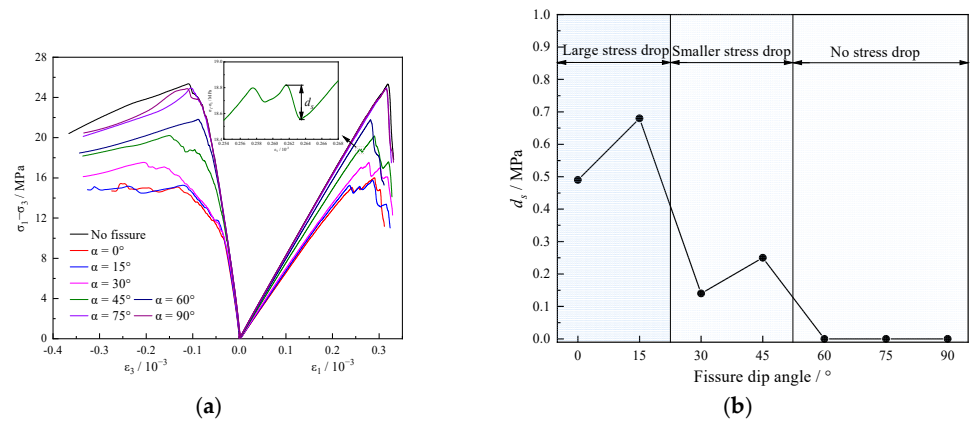


Figure 6. Stress-strain curve of symmetrical fissure-hole sandstone. (a) The stress-strain curve of 2a = 8 mm specimen; (b) the effect of fissure dip angle on stress drop amplitude.

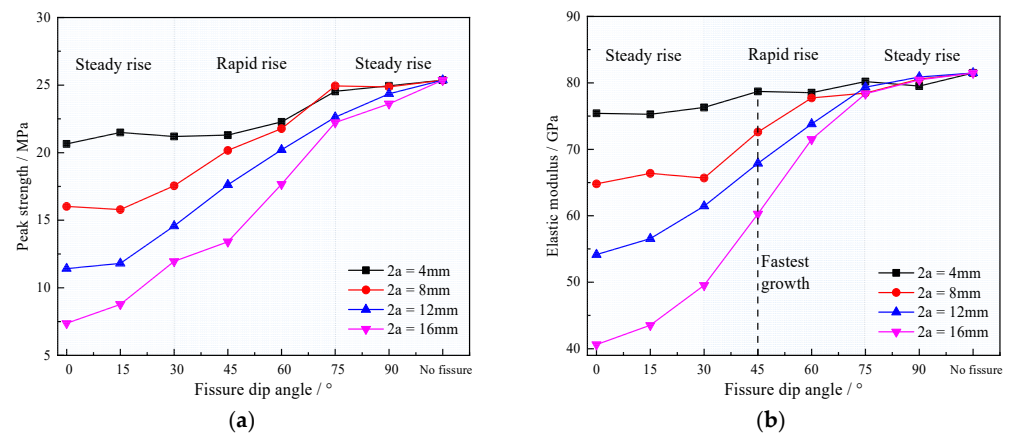


Figure 7. Effect of symmetrical fissure dip on strength parameters of hole-containing sandstone. (a) Peak strength; (b) elastic modulus.

Figure 8 shows the effect of fissure length on the strength parameters of sandstones containing pores. As depicted in Figure 8, there is an apparent linear decrease in both peak strength and elastic modulus of the specimens as fissure length increases. The slope of these linear regressions becomes steeper as fissure inclination decreases, with the best fit between peak strength and fissure length occurring at $\alpha = 0^\circ$ ($R_2 = 0.9992$). Conversely, $\alpha = 75^\circ$ and 90° exhibit the weakest linear fit between the elastic modulus and fissure length and a weaker negative correlation between peak strength and elastic modulus with increasing fissure length. This may be due to microcrack expansion within the specimen and variations in damage patterns. In summary, our results demonstrate that an increase in fissure length exacerbates the detrimental effect of symmetric fissures on the mechanical properties of hole-containing sandstones. However, the magnitude of this degradation decreases with increasing fissure angle.

4.2. Displacement Field Analysis

To study the effect of symmetric fissure morphology on the relative displacement of particles around a hole, specimens with 2a = 8 mm were selected to analyze the displacement field of particles near the hole with different fissure dip angles. As illustrated in Figure 9, the small arrow's color indicates the particle displacement's magnitude, while the large red arrow denotes its direction. Based on the size and direction of the particle displacement, it can be identified that the specimens primarily exhibit tensile and shear-tensile cracks.

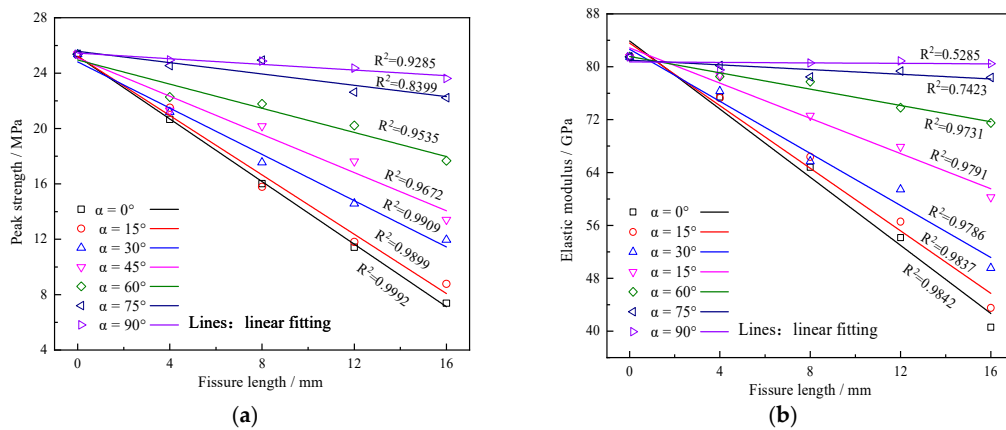


Figure 8. Effect of symmetrical fissure length on strength parameters of hole-containing sandstone. (a) Peak strength; (b) elastic modulus.

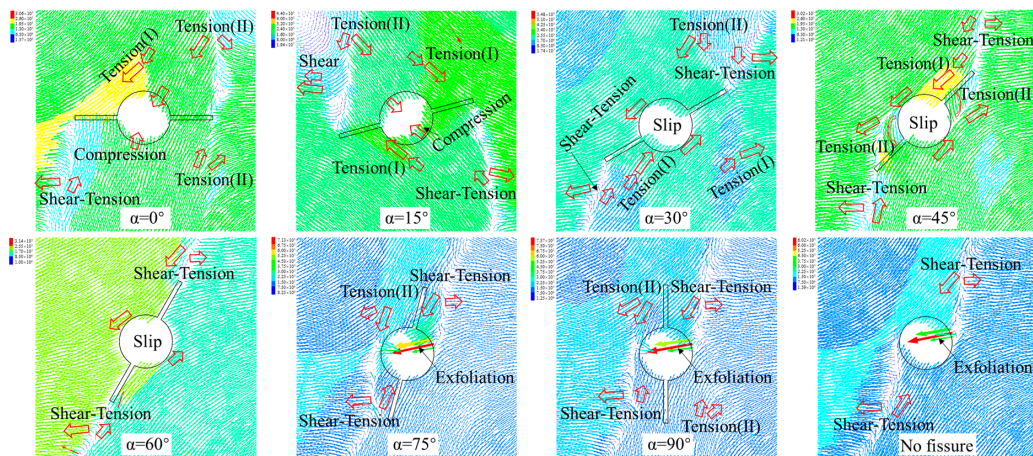


Figure 9. Displacement vector diagram of specimens with different fracture dip angles ($2a = 8$ mm).

Tensile cracks can be classified into two categories based on their causes. The first category is tensile cracks attributed to the displacement difference in the direction of particle movement, represented by Tension(I) in the diagram. These cracks are typically more minor in size and occur mainly around the hole of the specimen with small fissure dip angles ($\alpha = 0\sim 45^\circ$). The second category is tensile cracks caused by the opposite direction of particle transverse displacement, represented by Tension(II) in the diagram. These cracks primarily originate from the fissure tips, are usually larger, and can cause partial tensile failure of the specimen. Additionally, they are responsible for the hole and fissure tip penetration in specimens with fissure dip angles of 45° , 75° , and 90° . Shear-tensile cracks, indicated by Shear-Tension in the diagram, primarily result from particles displaced in opposite directions, with the angle between the particle displacement directions being obtuse. This often leads to particle slip and tearing, although overall shear-slip is still predominant. Moreover, the prominent cracks that eventually cause damage are all macroscopic shear-tensile cracks in the specimens.

The dip angle of fissures directly influences the deformation and failure of a hole. Particle displacement around the hole changes continuously with an increase in α , resulting in three primary forms of deformation and failure. At $\alpha = 0^\circ$ and 15° , compressive stress causes particles around the hole to move toward its interior, leading to shrinkage. At α values between 30° and 60° , shear failure is enhanced, and particle displacement on both sides of the hole is parallel and reversed, resulting in shear deformation. Finally, when α is at 75° and 90° , stress concentration on the hole wall causes particles to flake off towards the inside under compressive stress, leading to failure similar to that of a single hole non-fissure

specimen. Therefore, it can be concluded that the effect of symmetric fissure dip angle on particle displacement around the hole decreases as α increases.

To further investigate the effect of fissure length on the internal displacement field of the hole-containing sandstone, the displacement fields near the hole of specimens with different fissure lengths at $\alpha = 45^\circ$ were selected for analysis, as shown in Figure 10. When $2a = 4\text{ mm}$ and 16 mm , particles around the hole and fissures are displaced in opposite directions on the fissure direction, the hole and fissures are distorted by shear slip, and shear-tension cracks sprout from the fissure tip. When $2a = 12\text{ mm}$, the counterclockwise twisting of the particles near the hole wall produced tensile cracks through the hole and the fissure tips. Compared with the $2a = 8\text{ mm}$ specimen, the magnitude of the particle displacement near the hole was more significant, the displacement direction was closer to the hole, and the hole shrank inward. It can be seen that the increase in fissure length will intensify the deterioration effect of fissures on the rock mass around the hole, but this effect will be substantially weakened when the fissure length size is too large.

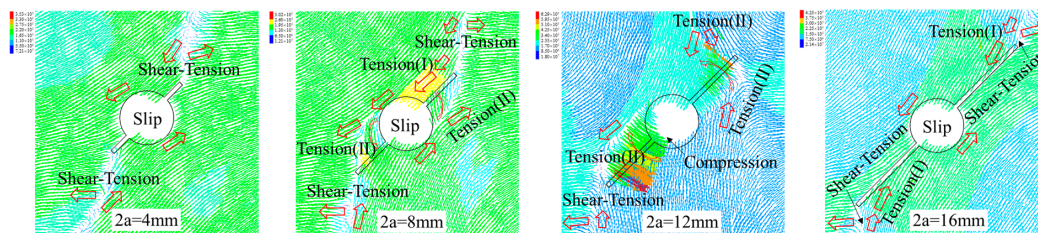


Figure 10. Displacement vector diagram of specimens with different fissure lengths ($\alpha = 45^\circ$).

4.3. Failure Mode Analysis

The initiation and propagation of microcracks inside the rock are essential factors leading to the final failure. Table 6 gives the initiation locations of microcracks in the hole-containing sandstone under different fissure morphologies. In contrast, C and H in the table indicate two forms of initiation, fissure tip initiation, and hole wall initiation. It is shown in the table that the change in the crack inclination makes the microcrack initiation location evolve from the crack tips to the hole wall. This is because the stress concentration location in the specimen evolves gradually from the fissure tip to the hole wall when the fissures are gradually parallel to the principal axial stress, which causes the microcrack initiation location to change.

Table 6. The location of micro-crack initiation under triaxial compression.

Parameter	$\alpha = 0^\circ$	$\alpha = 15^\circ$	$\alpha = 30^\circ$	$\alpha = 45^\circ$	$\alpha = 60^\circ$	$\alpha = 75^\circ$	$\alpha = 90^\circ$
$2a = 4\text{ mm}$	C	C	C	C	C	C	H
$2a = 8\text{ mm}$	C	C	C	C	C	H	H
$2a = 12\text{ mm}$	C	C	C	C	C	H	H
$2a = 16\text{ mm}$	C	C	C	C	C	H	H

The final failure modes of the hole-containing sandstone at different fissure dip angles are given in Figure 11, from which it can be seen that the failure modes of the specimens are mainly divided into four types as the fissure dip angle increases with the fissure length of 8 mm:

1. At $\alpha = 0^\circ, 15^\circ$, the prominent cracks all crack along the direction perpendicular to the symmetrical fissures and then respectively expand obliquely up (down) to the specimen boundary, showing mixed shear-tensile failure. In addition, secondary cracks sprouted on the upper and lower sides of the fissure tips and hole wall, and the secondary cracks all expanded roughly in the direction of the principal axial stress, which aggravated the tensile failure of the specimen.
2. At $\alpha = 30^\circ, 45^\circ$, the proper main crack obliquely extends upward (downward) to the specimen boundary, forming a triangular fragment. Moreover, the secondary cracks

all crack from the fissure tip along the direction perpendicular to the fissure, and then the extension direction turns toward the axial main stress direction. Compared with $\alpha = 0^\circ, 15^\circ$, the specimen's tensile failure degree is weakened, and the degree of shear failure is enhanced.

3. At $\alpha = 60^\circ$, the main crack is co-linear with the symmetric fissures, and the specimen eventually produces shear failure along the diagonal.
4. At $\alpha = 75^\circ$ and 90° , the failure modes of the specimens are similar to those of the single-hole fissure-free specimen, with the prominent cracks starting from the right (left) side of the hole wall and then expanding obliquely upward (downward), leading to shear failure of the specimens, however, due to the compressive stress, some of the tensile cracks penetrate the fissure tip to the hole wall, which is also reflected in the $\alpha = 45^\circ$ specimen, and the tensile failure of the specimens is slightly enhanced.

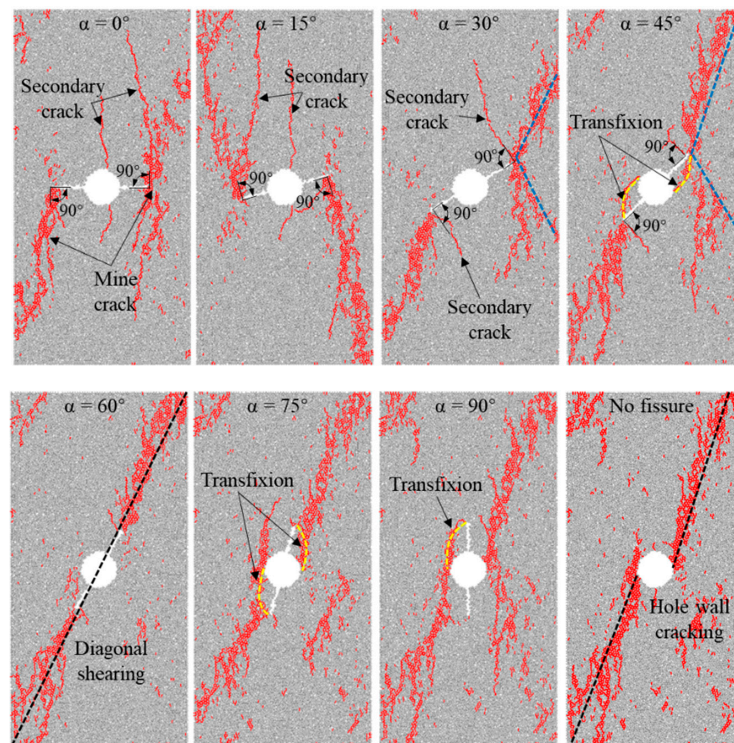


Figure 11. Effect of fissure dip angle on the final failure modes of the hole-containing sandstone ($2a = 8$ mm).

Figure 12 illustrates the relationship between fissure length and failure modes of specimens with a 45° fissure dip angle. The plot shows specimens experience shear failure along the diagonal when the fissure length is small ($2a = 4$ mm). At $2a = 8$ mm and 12 mm, the primary cracks form a triangular fragmentation with the specimen boundary. Secondary cracks perpendicular to the symmetric fracture are generated, and tensile cracks penetrate the rock bridges between the fracture tips and the hole. Tensile failure is more significant in the $2a = 12$ mm specimen, intensifying the fragmentation compared to the $2a = 8$ mm specimen. When $2a = 16$ mm, the number of cracks substantially decreases, and the main crack extends obliquely upward (or downward) from the fissure tip to the boundary of the specimen. This is due to the excessive size of the fissure, which weakens the deterioration effect of the fissure on the rock near the hole and enhances the edge effect. Thus, fissure length exacerbates the tensile failure of the specimens to some extent, but excessive fissure length weakens the effect of fissures on the rock around the hole.

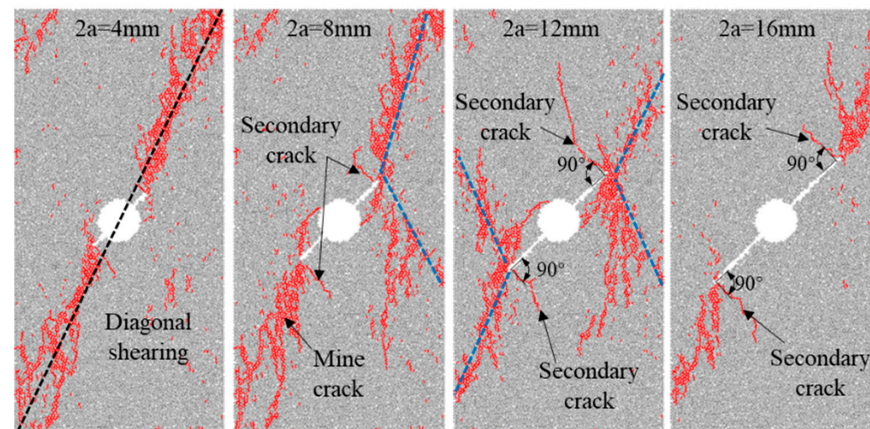


Figure 12. Effect of fissure length on the final failure modes of the hole-containing sandstone ($\alpha = 45^\circ$).

5. Discussion

The previous analysis reveals that symmetric fissures can hurt the mechanical properties of hole-containing sandstone. These properties, in turn, affect the rate and direction of crack propagation. When the mechanical properties are high, the cracks in the rock require tremendous pressure to propagate further. Conversely, crack propagation characteristics indicate the deformation and failure behavior of the rock. The quicker the rate of crack propagation, the lower the rock's strength and toughness. Therefore, it is necessary to discuss the relationship between crack propagation and the macroscopic mechanical properties of specimens during rock destruction and to reveal the microscopic characteristics of the effect of symmetric fissures on the deterioration of the mechanical properties of the hole-containing sandstone.

5.1. Relationship between Mechanical Properties and Crack Expansion

To examine the relationship between macroscopic mechanical properties, crack propagation, and stress field distribution during triaxial compression loading, we monitored changes in the number of microcracks using acoustic emission. In PFC simulations, the interactions between particles promote the initiation and propagation of microcracks. During this process, the released elastic waves are monitored by Acoustic Emission Sensor configured on the particles, enabling the simulation of rock acoustic emissions. To conserve space, we selected a specimen with $2a = 8 \text{ mm}$ and $\alpha = 45^\circ$ for analysis. Our findings shed light on the behavior of symmetrical fissure-hole sandstone specimens under these conditions.

Figure 13a–h shows the crack propagation and force chain distribution patterns with large fluctuations in microcracks and stress-strain curves. According to the growth rate of microcracks, the crack propagation process can be divided into three stages: crack initiation, development, and rapid crack propagation. During the a–b stage, there is a stress concentration at the tip of the fissure, which induces the initiation of microcracks near the fissure tip. As stress concentrations gradually extend toward the hole wall in stages b–e, the load-bearing properties of the rock sample are weakened in this area. This process also drives the development of microcracks near the defect. During stages c–d, tensile cracks penetrate the fissure and hole, accelerating crack growth and causing the stress to drop simultaneously. In stages e–h, the force chain thinning zone near the defects expands, leading to a significant reduction in the load-bearing capacity of the specimen after reaching peak strength and experiencing rapid crack expansion. During stages f–g, the crack propagation slows down, possibly due to the partial closure of microcracks under pressure. However, this short enhancement of mechanical properties is quickly followed by rapid destabilization and damage to the specimen. Therefore, as the stress concentration zone gradually expands from the fissure tip to the hole wall during the crack development stage, cracks propagate towards the hole wall with increasing σ_1 , resulting in a noticeable decrease in macroscopic mechanical properties. This phenomenon is similar

to the acoustic emission findings of Yang [14] for sandstone containing fissures and holes (with $2a = 2b = 8 \text{ mm}$). However, the stress drop in their study occurred early on due to a lack of lateral pressure effects.

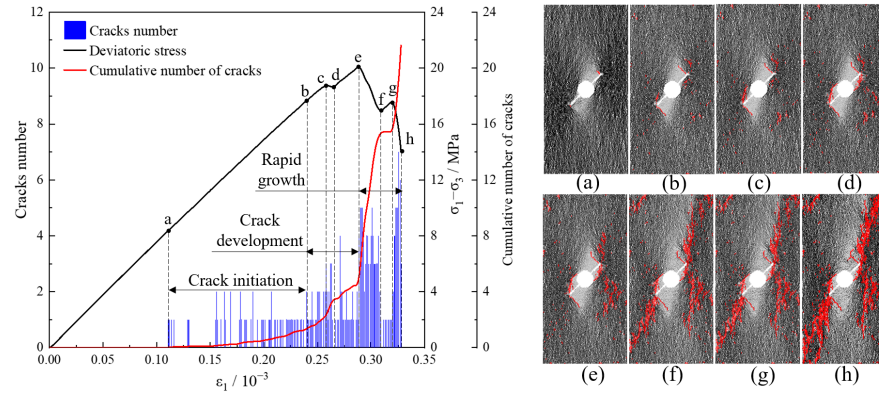


Figure 13. Symmetrical fissure-hole sandstone crack propagation process and force chain distribution ($2a = 8 \text{ mm}$, $\alpha = 45^\circ$). The subfigures (a)–(h) represent the crack extension pattern and microscopic force chain distribution corresponding to points a-h in the stress-strain curve.

5.2. Evolution Law of Microcrack Number

The compressional failure of rocks involves initiating and developing microcracks within the rock. Figure 14 illustrates how the dip angle and length of fissures relate to the evolution of the microcrack number. Figure 14a illustrates that for $\alpha = 0\sim 45^\circ$, the number of cracks shows a “step” growth trend in both the crack development and rapid growth phase. This mode shows more obvious tensile failure in the failure modes. In contrast, when $\alpha = 60\sim 90^\circ$, the number of cracks grows steadily in the crack development phase and steeply in the rapid growth phase, similar to the evolution of the number of cracks in the fissure-free specimen. The shear failure in the failure modes is also significant in this case. Figure 14b shows that when the fissure length is small ($2a = 4 \text{ mm}$), the crack growth pattern is consistent with that of the fissure-free specimen. However, for more considerable fissure lengths ($2a = 16 \text{ mm}$), the mechanical properties of the specimen decrease, and the number of cracks decreases as well. It can be inferred that the evolution law of crack number corresponds to the mechanical properties and failure modes. When the dip angle of fissures is slight, the deterioration effect on the mechanical properties of the surrounding rock mass by symmetric fissures around the hole is more significant. The fluctuation of crack evolution is vital, which is exacerbated by an increase in fissure length.

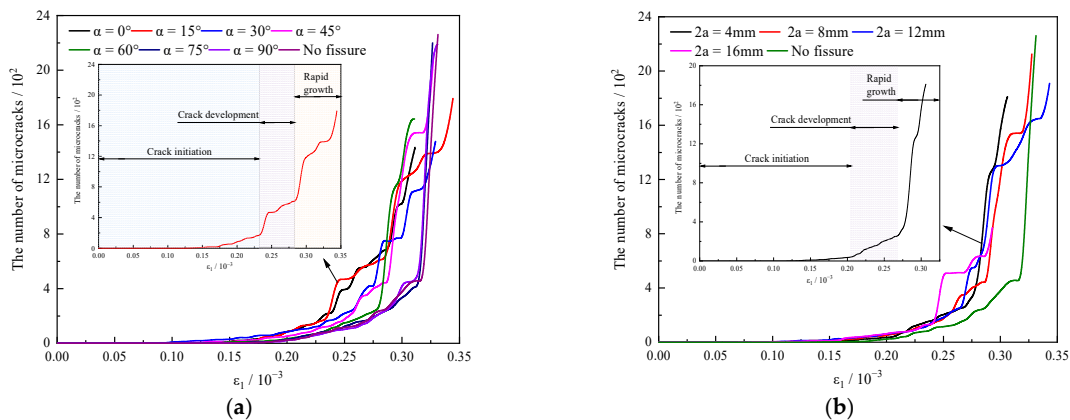


Figure 14. Relationship between symmetric fissures and the evolution of microcracks. (a) Microcrack evolution law for specimens with different fissure dip angles ($2a = 8 \text{ mm}$); (b) microcrack evolution law for specimens with different fissure lengths ($\alpha = 45^\circ$).

6. Conclusions

This paper explores the effect of symmetrical fissure morphology on the mechanical properties of hole-containing sandstone by developing models using granular flow program PFC2D. Furthermore, several key conclusions about the relationship between fissure morphology and sandstone strength exist.

1. The deterioration effect of symmetric fissures on hole-containing sandstone can be controlled by increasing the fissure dip angle, suppressing the stress drop phenomenon. However, increasing the fissure length exacerbates the deterioration effect. The experimental findings indicate that the peak strength and elastic modulus of symmetrical fissure-hole sandstone are positively correlated with the fissure dip angle and negatively correlated with the fissure length within the experimental range.
2. The effect of a symmetrical fissure dip angle on the displacement field near the hole decreases with increasing dip angle while increasing fissure length exacerbates the effect of a fissure on the displacement field; the opposing transverse displacement of particles is the dominant factor for local tensile failure of the specimens and fissure penetration with the hole; as the fissure inclination increases, three damage patterns of compression, slip, and spalling occur in the hole in turn.
3. The symmetrical fissure-hole sandstone failure modes under conventional triaxial compression are all mixed shear-tension failures. As the angle between the fissures and the principal vertical stress increases, the degree of tensile failure weakens while the degree of shear failure increases. Moreover, the location of crack initiation shifts from the fissure tip towards the hole wall.
4. During the crack development stage of symmetrical fissure-hole sandstone specimens, the extension of the stress concentration zone drives rapid crack growth. It exhibits a stress drop in the macroscopic mechanical properties, followed by the evolution of the stress field with loading and rapid expansion of microcracks, eventually leading to destabilization and damage of the specimen.

Author Contributions: Methodology, H.G. and Z.W.; validation, P.S. and Z.Z.; investigation, Z.W. and L.X.; data curation, B.F. and P.S.; writing—original draft preparation, H.G. All authors have read and agreed to the published version of the manuscript.

Funding: This research received no external funding.

Data Availability Statement: The data presented in this study are available on request from the corresponding author.

Conflicts of Interest: The authors declare no conflict of interest.

References

1. Zhao, E.B.; Li, K.N.; Yang, X.; Deng, N. Speculum Observation and Trajectory Measurement in Gas Extraction Drilling: A Case Study of Changling Coal Mine. *Geofluids* **2021**, *2021*, 5545067. [[CrossRef](#)]
2. Shuchen, L.; Tengfei, M.; Yujing, J.; Shucui, L.; Luchen, Z. Model tests on deformation and failure laws in excavation of deep rock mass with multiple fracture sets. *Chin. J. Geotech. Eng.* **2016**, *38*, 987–995.
3. Ze, Z.; Chuanqu, Z.; Qingfeng, L. Failure mechanism and stability control of roof roadway in fractured zone. *J. China Coal Soc.* **2017**, *42*, 1400–1407. [[CrossRef](#)]
4. Junhua, Z.; Kun, Y.; Kai, F.; Tongbin, Z.; Dongwei, Q. Effect of fissure on mechanical and damage evolution characteristics of sandstone containing hole defect. *J. Cent. South Univ.* **2019**, *50*, 968–975.
5. Chaojiong, H.; Xiangyu, W.; Jianbiao, B.; Ning kang, M.; Wenda, W. Basic theory and technology study of stability control for surrounding rock in deep roadway. *J. China Univ. Min. Technol.* **2021**, *50*, 1–12. [[CrossRef](#)]
6. Bobet, A.; Einstein, H.H. Fracture coalescence in rock-type materials under uniaxial and biaxial compression. *Int. J. Rock Mech. Min. Sci.* **1998**, *35*, 863–888. [[CrossRef](#)]
7. Chuang, Z.; Jianxin, T.; Junyang, T.; Chenlin, L. Experimental study of influences of pore number and pore size on mechanical properties of marble. *Rock Soil Mech.* **2017**, *38*, 41–50. [[CrossRef](#)]
8. Lajtai, E.Z.; Lajtai, V.N. The collapse of cavities. *Int. J. Rock Mech. Min. Sci. Geomech. Abstr.* **1975**, *12*, 81–86. [[CrossRef](#)]
9. Lin, P.; Wong, R.H.C.; Tang, C.A. Experimental study of coalescence mechanisms and failure under uniaxial compression of granite containing multiple holes. *Int. J. Rock Mech. Min. Sci.* **2015**, *77*, 313–327. [[CrossRef](#)]

10. Wong, R.H.C.; Tang, C.A.; Chau, K.T.; Lin, P. Splitting failure in brittle rocks containing pre-existing flaws under uniaxial compression. *Eng. Fract. Mech.* **2002**, *69*, 1853–1871. [[CrossRef](#)]
11. Yanhua, H.; Shengqi, Y.; Yang, J.; Xiaoping, Z.; Feng, G. Experimental study on mechanical behavior of rock-like materials containing pre-existing intermittent fissures under triaxial compression. *Chin. J. Geotech. Eng.* **2016**, *38*, 1212–1220.
12. Yu, Z.; Daguo, Q.; Chaolin, W.; Mingyang, T.; Jing, B. Experimental study and particle flow modeling on 3D cracking behavior of rock-like samples with an embedded flaw. *Eur. J. Environ. Civ. Eng.* **2022**, *26*, 6897–6913.
13. Zhaohui, W.; Wenchao, S.; Yanting, S.; Hao, G. Surface deformation field and fracture propagation mechanism of rock-like samples with pre-existing fracture. *Coal Sci. Technol.* **2022**, 1–11. [[CrossRef](#)]
14. Yang, S.-Q.; Liu, X.-R.; Li, Y.-S. Experimental analysis of mechanical behavior of sandstone containing hole and fissure under uniaxial compression. *Chin. J. Rock Mech. Eng.* **2012**, *31*, 3539–3546.
15. Modiriasari, A.; Bobet, A.; Pyrak-Nolte, L.J. Active Seismic Monitoring of Crack Initiation, Propagation, and Coalescence in Rock. *Rock Mech. Rock Eng.* **2017**, *50*, 2311–2325. [[CrossRef](#)]
16. Zhu, T.-T.; Jing, H.-W.; Su, H.-J.; Yin, Q. Experimental investigation on mechanical behavior of sandstone with coupling effects under uniaxial compression. *J. China Coal Soc.* **2015**, *40*, 1518–1525. [[CrossRef](#)]
17. Li, X.-H.; Niu, Z.-J.; Yao, Q.-L.; Wang, W.-N.; Yu, L.-Q. Particle flow analysis of crack propagation characteristics of hole-type trident cracks sandstone. *J. China Coal Soc.* **2020**, *45*, 3735–3747. [[CrossRef](#)]
18. Zeinab, A.; Mansour, S.; Faham, T.; Luming, S. Experimental and numerical investigations on crack development in 3D printed rock-like specimens with pre-existing flaws. *Eng. Fract. Mech.* **2020**, *241*, 107396.
19. Sharafisafa, M.; Nazem, M. Application of the distinct element method and the extended finite element method in modelling cracks and coalescence in brittle materials. *Comput. Mater. Sci.* **2014**, *91*, 102–121. [[CrossRef](#)]
20. Wang, X.-F.; Xia, Z.-J.; Li, P.; Liu, H.-N. Numerical Study on Strength and Failure Behavior of Rock with Composite Defects under Uniaxial Compression. *Energies* **2021**, *14*, 4418. [[CrossRef](#)]
21. Yao, D.-H.; Jiang, N.; Wang, X.-J.; Jia, X.-D.; Lv, K. Mechanical behaviour and failure characteristics of rocks with composite defects of different angle fissures around hole. *Bull. Eng. Geol. Environ.* **2022**, *81*, 290. [[CrossRef](#)]
22. Sherong, Z.; Bo, S.; Chao, W.; Lei, Y. Discrete element analysis of crack propagation in rocks under biaxial compression. *Chin. J. Rock Mech. Eng.* **2013**, *32*, 3083–3091.
23. Chong, S.; Weiya, X. *Particle Flow Numerical Simulation Skills and Practice*; China Building Industry Press: Beijing, China, 2015; pp. 6–15.
24. Itasca, C. PFC (particle flow code in 2 and 3 dimensions), version 5.0 [User's manual]. *Numer. Anal. Methods Geomech.* **2014**, *32*, 189–213.
25. Huiqiang, D. *Study on the Fatigue Failure and Fractal Characteristics of Coal Subjected to Triaxial Cyclic Loading*; Shandong University of Science and Technology: Qingdao, China, 2018.
26. Jiang, M.-J.; Chen, H.; Zhang, N.; Fang, R. Distinct element numerical analysis of crack evolution in rocks containing pre-existing double flaw. *Rock Soil Mech.* **2014**, *35*, 3259–3268+3288. [[CrossRef](#)]
27. Yuchi, W.; Yong, Y.; Zhongzheng, Z.; Jun, H.; Zhiguo, X.; Bing, Y. Mechanical properties and failure characteristics of combined hole rocks with different dip angles based on PFC2D. *Min. Metall.* **2022**, *31*, 132–139.
28. Yang, S.-Q.; Yin, P.-F.; Zhang, Y.-C.; Chen, M.; Zhou, X.-P.; Jing, H.-W.; Zhang, Q.-Y. Failure behavior and crack evolution mechanism of a non-persistent jointed rock mass containing a circular hole. *Int. J. Rock Mech. Min. Sci.* **2019**, *114*, 101–121. [[CrossRef](#)]

Disclaimer/Publisher's Note: The statements, opinions and data contained in all publications are solely those of the individual author(s) and contributor(s) and not of MDPI and/or the editor(s). MDPI and/or the editor(s) disclaim responsibility for any injury to people or property resulting from any ideas, methods, instructions or products referred to in the content.